

1 **The Predictive Skills of Elastic Coulomb Rate-and-state Aftershock**
2 **Forecasts During the 2019 Ridgecrest, California, Earthquake Sequence**

3
4 **S. Mancini** ^{1,2}, **M. Segou** ², **M. J. Werner** ¹, and **T. Parsons** ³

5 ¹ School of Earth Sciences, University of Bristol, BS8 1RL Bristol, UK

6 ² British Geological Survey, Lyell Centre, EH10 4AP, Edinburgh, UK

7 ³ United States Geological Survey, Moffett Field, California, USA

8
9 Corresponding author: Simone Mancini (simone.mancini@bristol.ac.uk)

10
11
12
13
14
15
16
17
18
19
20
21
22
23

24 **Abstract**

25 Operational earthquake forecasting protocols commonly use statistical models for their
26 recognized ease of implementation and robustness in describing the short-term spatiotemporal
27 patterns of triggered seismicity. However, recent advances on physics-based aftershock
28 forecasting reveal comparable performance to the standard statistical counterparts with
29 significantly improved predictive skills when fault and stress field heterogeneities are considered.
30 Here, we perform a pseudo-prospective forecasting experiment during the first month of the 2019
31 Ridgecrest (California) earthquake sequence. We develop seven Coulomb rate-and-state models
32 that couple static stress change estimates with continuum mechanics expressed by the rate-and-
33 state friction laws. Our model parametrization supports a gradually increasing complexity; we start
34 from a preliminary model implementation with simplified slip distributions and spatially
35 homogeneous receiver faults to reach an enhanced one featuring optimized fault constitutive
36 parameters, finite-fault slip models, secondary triggering effects, and spatially heterogenous
37 planes informed by pre-existing ruptures. The data-rich environment of Southern California allows
38 us to test whether incorporating data collected in near real-time during an unfolding earthquake
39 sequence boosts our predictive power. We assess the absolute and relative performance of the
40 forecasts by means of statistical tests used within the Collaboratory for the Study of Earthquake
41 Predictability (CSEP) and compare their skills against a standard benchmark ETAS model for the
42 short (24 hours after the two Ridgecrest mainshocks) and intermediate-term (one month). Stress-
43 based forecasts expect heightened rates along the whole near-fault region and increased expected
44 seismicity rates in Central Garlock Fault. Our comparative model evaluation supports that faulting
45 heterogeneities coupled with secondary triggering effects are the most critical success components
46 behind physics-based forecasts, but also underlines the importance of model updates incorporating

47 near real-time available aftershock data reaching better performance than standard ETAS. We
48 explore the physical basis behind our results by investigating the localized shut down of pre-
49 existing normal faults in the Ridgecrest near-source area.

50

51 **Introduction**

52 On 4 July 2019, a Mw 4.0 earthquake occurred in the Searles Valley (Southern California)
53 and was followed within ~30 minutes by a Mw 6.4 event. Just 34 hours later, on 6 July, a Mw 7.1
54 earthquake struck near the town of Ridgecrest approximately 10 km NE of the Mw 6.4 epicenter.
55 The 2019 Ridgecrest earthquakes belong to the Eastern California Shear Zone (ECSZ), where large
56 magnitude seismicity had not been observed since the 1999 Mw 7.1 Hector Mine event. The two
57 earthquakes nucleated on a system of orthogonal strike slip faults (Figure 1): northeast-trending
58 left-lateral for the Mw 6.4 event and northwest-trending right-lateral for the Mw 7.1 mainshock.
59 The activated area is located in the vicinity of the Airport Lake and Little Lake fault zones,
60 characterized by distributed faulting with mainly right-lateral strike slip and normal kinematics
61 (*Bryant, 2017*). The resulting cascade of aftershocks involved several subparallel faults that
62 cumulatively exceeded 75 km in length (*Barnhart et al., 2019; Ross et al., 2019; Chen et al., 2020*).

63 The Ridgecrest area has previously experienced moderate magnitude earthquakes,
64 including the 1982 Mw 5.2 Indian Wells Valley event and the 1995-1996 sequence with three M5+
65 shocks, the first two of which occurred five weeks apart. The 1995 earthquakes exhibited similar
66 complexity to the 2019 events, with triggered seismicity on normal and strike-slip northwest and
67 northeast trending faults (*Hauksson et al., 1995*).

68 The tectonic setting of the epicentral region, bounded by the Garlock system to the south
69 and extending towards the Owens Valley fault to the north (Figure 1), where moderate to large

70 magnitude earthquakes occurred in the last ~150 years (including the 1872 $M \approx 7.5$ Owens Valley
71 earthquake), immediately raised severe concerns on whether the occurrence of the July 2019
72 events could promote the nucleation of large events on nearby faults, as previously observed in the
73 ECSZ (e.g. the 1992 Landers sequence).

74 Among the physics-based approaches employed to model the expected rate of triggered
75 seismicity due to fault-to-fault interactions, Coulomb rate-and-state (CRS) forecasts combine the
76 calculation of the static stress changes cast by an earthquake in the surrounding crustal volume
77 (*Harris & Simpson, 1992*) with laboratory-derived rate-and-state constitutive laws (e.g. *Dieterich,*
78 *1994*) that describe the fault's frictional response to the imparted stresses. Recent work on the
79 improvement of such physics-based forecasts within the 2016-2017 Central Apennines (Italy)
80 earthquake sequence showed that the predictive skills of CRS models increase when crustal and
81 stress field heterogeneity resulting from past focal mechanisms and secondary earthquake
82 triggering is considered (*Mancini et al., 2019*). The 2019 Ridgecrest sequence presents a unique
83 opportunity to further test the performance of CRS forecasts and advance our understanding of
84 model features that improve short-term aftershock forecasts in high-hazard settings with complex
85 rupture patterns and diverse population of triggered seismicity. In the era of machine learning
86 catalogs that promise future improvements in real-time earthquake detection (e.g. *Ross et al., 2018;*
87 *Mousavi et al., 2019*), we investigate whether physics-based forecasts can benefit from the
88 inclusion of sequence-specific data. Hence, we extend previous work by testing if the predictive
89 power of Coulomb rate-and-state forecasts increases when we update fault models using evolving
90 aftershock data.

91 Here we perform a pseudo-prospective experiment, that is, the issued models follow
92 approximately the evolution of near real-time data availability and quality. Focusing on their

93 overall predictive power and their spatial consistency, we present the absolute and relative
94 performance of the forecasts for the first month following the Mw 6.4 Searles Valley earthquake,
95 making use of the well-established evaluation metrics introduced by the Collaboratory for the
96 Study of Earthquake Predictability (CSEP – *Jordan, 2006; Michael & Werner, 2018*). To
97 benchmark the CRS models, we produce a basic realization of a statistical Epidemic Type
98 Aftershock Sequence model (ETAS – *Ogata, 1998*), which currently represents the most robust
99 and widely used modelling tool for Operational Earthquake Forecasting (OEF; *Jordan et al., 2011,*
100 2014).

101

102 **Data**

103 We develop the earthquake forecasts on a testing region (Figure 1) centered on the Mw 7.1
104 mainshock epicenter and extending equally E-W and N-S for ~160 km (three time its rupture
105 length). We discretize the models using a three-dimensional grid with 2 km spacing between 0-28
106 km of depth. Our target seismicity is the real time catalog of 1812 M2.5+ aftershocks reported in
107 the USGS Advanced National Seismic System Comprehensive Catalog (ComCat; *Guy et al., 2015*)
108 for the month following the Mw 6.4 Searles Valley event (testing phase, July 4th – August 4th
109 2019). As a pre-Ridgecrest learning phase (to calibrate models) we consider the seismicity between
110 January 1st 1981 – July 3rd 2019 by merging the 1981-2018 relocated catalog by *Hauksson et al.*
111 (2012) with the ComCat events covering the last six months before the Ridgecrest sequence (43986
112 events in total with M2.5+). While we adopt the catalog of focal mechanisms by *Yang et al. (2012)*
113 as evidence of the past local rupture styles in the testing region, we use the focal mechanism
114 solutions from the Southern California Earthquake Data Center (SCEDC) as a real-time database.
115 To constrain the faulting style on the main regional faults, we use the rupture parameters reported

116 in the third version of the Uniform California Earthquake Rupture Forecast (UCERF3; *Dawson,*
 117 2013), and we assign the larger scale off-fault rupture kinematics using the smoothed stress
 118 inversion from focal mechanisms and topography by *Luttrell and Smith-Konter* (2017), which is
 119 one of the available SCEC Community Stress Models (CSM).

120 To calculate the static coseismic stress changes after the Mw 7.1 mainshock we use the
 121 preliminary finite-fault slip model version issued on the USGS event information webpage, which
 122 provides near real-time automated source characterization. For the Mw 6.4 event and for all those
 123 earthquakes with a focal mechanism solution, we create a synthetic uniform slip distribution within
 124 a planar surface implementing the empirical equations of *Wells and Coppersmith* (1994) to
 125 calculate the approximate fault dimensions and the relation by *Hanks and Kanamori* (1979) to
 126 estimate the amount of slip given the event magnitude.

127

128 **Methods**

129 **Coulomb rate-and-state modelling**

130 Among the sources of stress perturbations, our CRS models include static stress changes
 131 and do not account for the effect of other known physical mechanisms such as dynamic stress
 132 changes, afterslip or poro-elastic effects that may as well contribute to the triggering process at
 133 different spatiotemporal scales.

134 For the calculation of the Coulomb stress changes (ΔCFF) we assume an elastic halfspace
 135 medium (*Okada, 1992*) with shear modulus of 30 GPa and Poisson's ratio $\nu=0.25$ as representative
 136 values for the upper crust. We adopt the definition of *Rice* (1992):

$$137 \quad \Delta CFF = \Delta\tau + \mu'(\Delta\sigma), \quad (1)$$

138 where $\Delta\tau$ is the change in shear stress resolved on a given fault geometry (commonly known as
 139 “receiver fault”) and set positive in direction of fault slip, $\Delta\sigma$ is the change in normal stress
 140 (positive when the fault is unclamped), $\mu' = \mu(1 - B)$ is the effective coefficient of friction, with
 141 B the Skempton’s coefficient describing pore pressure changes in response to a change in applied
 142 stress. Here, all developed and tested models feature $\mu' = 0.4$ (Toda *et al.*, 2005), but we address
 143 the uncertainty on μ' values in the supplemental material.

144 As the Coulomb stress hypothesis alone does not account for the time dependency of
 145 seismicity, to estimate the expected rates of earthquake production we choose to couple the
 146 coseismic static stress change calculations with rate-and-state friction constitutive laws, as they
 147 have so far represented a widely used and successful physical framework. Although more recent
 148 reviews of the rate-and-state model have been proposed (e.g. *Heimisson and Segall*, 2018), our
 149 approach implements the standard formulation by *Dieterich* (1994). According to the latter, the
 150 spatiotemporal seismicity rate evolves as:

$$151 \quad R(t, x, y) = \frac{r_0(x, y)}{\gamma(t)\dot{\tau}}, \quad (2)$$

152 where r_0 represents the background seismicity rate, $\dot{\tau}$ is the secular shear stressing rate (that is, it
 153 is assumed to remain unvaried) and γ is a variable that under stable conditions corresponds to:

$$154 \quad \gamma_0 = \frac{1}{\dot{\tau}}. \quad (3)$$

155 When a stress perturbation is applied to the population of receiver faults, the state variable
 156 instantaneously assumes a new value:

$$157 \quad \gamma_n = \gamma_{n-1} \exp\left(\frac{-\Delta S}{A\sigma}\right), \quad (4)$$

158 where $A\sigma$ is the effective normal stress acting on the receiver fault, ΔS is the stress imparted by
 159 the earthquake, and γ_n and γ_{n-1} represent the values of the γ variable before and after the stress

160 change, respectively. While in the *Dieterich* (1994) formulation the applied stress change is the
 161 shear stress change, CRS modelling usually assumes it to be a “modified” Coulomb stress change
 162 (*Dieterich et al.*, 2000) that also includes the contribution of the effective normal stress changes.
 163 This is achieved by considering $S = \tau - (\mu - \alpha)(1 - B)\sigma$, with α a positive non-dimensional
 164 constitutive parameter controlling perturbations in normal stress (*Linker & Dieterich*, 1992). To
 165 approximate S in equation (4) to the Coulomb stress change as traditionally defined in equation
 166 (1), we assume that $\mu' = (\mu - \alpha)(1 - B)$.

167 *Dieterich* (1994) and *Dieterich et al.* (2000) show that the state variable evolves as:

$$168 \quad d\gamma = \frac{1}{A\sigma} [dt - \gamma dS]. \quad (5)$$

169 Following equation (4), a positive stress change causes a drop of the γ value and consequently a
 170 higher earthquake rate according to equation (2). However, the seismicity rate eventually recovers
 171 as the state variable evolves in time according to *Dieterich* (1994):

$$172 \quad \gamma_{n+1} = \left(\gamma_n - \frac{1}{\dot{\tau}} \right) \exp\left(\frac{-\Delta t \dot{\tau}}{A\sigma} \right) + \frac{1}{\dot{\tau}}, \quad (6)$$

173 where Δt is the time step.

174 In the *Dieterich's* (1994) rate-and-state framework, the ratio between the normal stress $A\sigma$ and the
 175 secular shear stressing rate $\dot{\tau}$ is the aftershock recovery time (t_a) required for the seismicity rate R
 176 to return to the background value r_0 through an Omori-like decay:

$$177 \quad t_a = \frac{A\sigma}{\dot{\tau}}. \quad (7)$$

178 Here, we present seven models for Coulomb rate-and-state forecasts, that we implement
 179 using the parallel code by *Cattania and Khalid* (2016). We issue successive realizations by
 180 gradually introducing one or more levels of complexity in terms of model parameterizations and
 181 fault and source heterogeneities (*i.e.* each model preserves all the characteristics of the previous

182 one, changing/introducing only those specified in its denomination). Using a more technical term,
183 we conduct a ‘pseudo-prospective’ experiment where we test the effectiveness of different
184 Coulomb rate-and-state forecasts that evolve from preliminary to progressively more elaborated
185 parameterizations according to near-real time data availability. We update all the forecasts at time
186 windows (Δt) of 24 hours or when a $M6+$ event occurs (whichever comes sooner), for a total
187 forecast horizon of 1 month. It is worth pointing out that we do not parameterize models using the
188 same data sample they are meant to forecast and that we estimate the next day seismicity rates out
189 of sample. In other words, the models neither know nor use any next-day seismicity information
190 to tune their components. Here, all CRS models are developed simultaneously, so that our
191 modelling choices for the more enhanced realizations are not biased by the performance of the
192 earlier versions. CRS model characteristics are summarized in Table 1.

193 The first CRS model, *CRS1-basic*, is the most preliminary version featuring: (1) stress
194 changes imparted only by the M_w 6.4 and M_w 7.1 events, for which we implement a uniform slip
195 distribution tapered at the edges of the fault from the real-time kinematic parameters provided by
196 the SCEDC; (2) simplified receiver plane geometry, spatially uniform (SUP) and parallel to the
197 M_w 7.1 fault which is consistent with the main regional regime; (3) spatially variable background
198 rate (r_0) after stochastic declustering (*Zhuang et al.*, 2002) of the learning phase seismicity catalog
199 (1981-2019), smoothed in space using the adaptive kernel method of *Helmstetter et al.* (2007); (4)
200 rate-and-state parameters averaged from the previous work of *Toda et al.* (2005), who investigated
201 the fingerprint of stress transfer by tuning parameters to Southern California seismicity during a
202 subset (1986-2003) of our learning phase window.

203 In *CRS2-optimized* we optimize the constitutive parameters during the learning phase
204 catalog by maximizing the log-likelihood function of *Zhuang et al.* (2012). The grid search spans

205 [0.01-0.1] MPa for $A\sigma$ and [1-300] years for t_a and includes the stress changes due to the past
206 M4+ events within the testing region during the 1981-2019 window. To account for early catalog
207 incompleteness, the fitting routine ignores the first 20 minutes after each stress-perturbing
208 earthquake, corresponding to the best fitting Omori c-value obtained for our ETAS model (see
209 Table S1).

210 CRS3-FFM/SSI introduces two features, namely the implementation of the near real-time
211 USGS finite-fault slip model (FFM) for the Mw 7.1 mainshock (while no slip inversion was
212 available for the Mw 6.4 event) and a first order structural heterogeneity of the receiver faults
213 (spatially variable planes – SVP) in the form of: (1) in off-fault regions, planes informed from the
214 smoothed stress inversion (SSI) from focal mechanisms and topography by *Luttrell and Smith-*
215 *Konter* (2017), and (2) at the fault-specific scale, mapped UCERF3 fault geometries with
216 kinematic parameters assigned following the USGS Fault Database in polygons extending ± 2.5
217 km around the rupture traces, with the exception of the Garlock Fault System where we consider
218 a 5 km buffer. The inclusion of UCERF3 rupture parameters allows accounting for well-known
219 extensional normal faults, such as the Kern Canyon and Tank Canyon, oblique-normal faults such
220 as the Independence Fault, right-lateral faults such as the Owens Valley, and left-lateral faults
221 related with the Garlock Fault System.

222 To resolve the evolving coseismic stress field in greater detail, CRS4-*secondary*
223 incorporates secondary triggering effects due to the stress changes following each M2.5+
224 aftershock. Except for the Mw 7.1 mainshock, which has an associated finite-fault model, we
225 implement uniform slip distributions from the SCEDC real-time catalog of focal mechanisms with
226 random selection of nodal planes, and we adopt a magnitude-dependent isotropic stress field for
227 all those events without any available rupture characterization (*Chen et al.*, 2013):

228
$$\Delta\text{CFF} = \frac{M_0}{6\pi r^3}, \quad (8)$$

229 In *CRS5-past_FMs* we introduce the representation of the second order structural
 230 complexities by resolving the stress changes on the diverse small-scale receiver fault populations
 231 of the area informed from pre-sequence focal mechanisms (1981-2019). We assign kinematic
 232 rupture parameters to each grid cell hosting at least one focal mechanism following a 3D nearest
 233 neighbor association and using the focal plane provided by the *Yang et al.* (2012) catalog.

234 The preliminary slip model version available on the USGS event webpage reaches a depth
 235 of 28 km and is explicitly affected by (1) a deep (~ 23 km) slip patch artifact on the north-western
 236 fault edge, and (2) an excessive fault length of about 160 km, extending well beyond the Garlock
 237 Fault to the SE and the Independence Fault to the NW. To overcome the limitations imposed by
 238 this near real-time data product, in model *CRS6-eFFM* we edit the USGS model (eFFM) by setting
 239 the rupture length according to the ShakeMap fault trace and extrapolating a vertical extension of
 240 17 km using the empirical relations of *Wells and Coppersmith* (1994). We chose to include both
 241 results to highlight the importance of real-time data quality control for automated operational
 242 forecasting.

243 *CRS7-new_FMs* is the most complex among our physics-based forecasts. In this model,
 244 we make use of those fault planes that are gradually revealed by aftershocks to resolve the evolving
 245 near-source coseismic stress changes. Here, the available real-time SCEDC focal mechanism of a
 246 given aftershock replaces the receiver plane earlier assigned to the relative grid point following a
 247 criterion of proximity to the center of its cell. We update the 3D receivers' matrix by performing
 248 such nearest neighbor re-assignment of aftershock nodal planes every time the forecast is updated.

249 We also present three additional sensitivity tests. First, to evaluate the effect of real-time
 250 data selection, we produce an alternative model version, *CRS7-usgs*, where we use the USGS

251 catalog of focal mechanisms for both the computation of the synthetic slip models and the receiver
252 faults update instead of the SCEDC one. This choice is motivated by the discrepancies between
253 the kinematic parameters of the mainshocks reported in real-time by the SCEDC and the USGS,
254 with special concern about the Mw 6.4 earthquake ($\sim 20^\circ$ difference in strike). Moreover, we assess
255 how the overall spatial performance of our more complex CRS realization changes when the r_0
256 value in equation (2) is defined by means of an undeclustered seismicity catalog (known as
257 ‘reference rate’). We perform this test in the wake of rederivations of the Dieterich’s model
258 suggesting that initial conditions for populations of seismic sources should also account for the
259 long-term seismicity interactions (*Heimisson, 2019*). Finally, we test the effect of implementing a
260 different coefficient of effective friction in model CRS7-*new_FMs*.

261

262 **The ETAS model**

263 The Epidemic Type Aftershock Sequence (ETAS) model was first introduced by *Ogata*
264 (1988) to describe the occurrence times and magnitudes of triggered seismicity and it was
265 successively extended into the spatial domain by *Ogata* (1998). Given their relatively simple
266 formulations and considerable performance, different versions of ETAS models are currently
267 employed by government agencies in several countries, including California (*Field et al., 2017*),
268 Italy (*Marzocchi et al., 2014*), New Zealand (*Gerstenberger and Rhoades, 2010*), and Japan (*Omi*
269 *et al., 2019*). Past and present initiatives, such as the Working Group of California Earthquake
270 Probabilities (WGCEP), Uniform California Earthquake Rupture Forecast (UCERF) and the
271 Collaboratory for the Study of Earthquake Probability (CSEP) tested the predictive skills of ETAS
272 models under different implementations for short- and long-term time horizons supporting that
273 moderate events in California occur near locations of small earthquakes (e.g. *Werner et al., 2011*)

274 and that the inclusion of the triggering potential of small magnitude events improves forecast
 275 performance (*Helmstetter et al., 2006*). Since our goal is to measure any improvement in the stress-
 276 based models, here we implement a standard ETAS version (*Seif et al., 2017*) to be used as
 277 benchmark and we acknowledge that a better performance may be reached by other ETAS
 278 formulations.

279 The ETAS model assumes that: (1) each event produces a population of direct offspring
 280 earthquakes (whose abundance depends on the parent’s magnitude) that follow an Omori-like
 281 decay, (2) seismicity is modelled as a point process that unfolds according to a stochastic branching
 282 process, (3) the magnitude of each triggered earthquake can exceed that of its direct parent event.
 283 The ETAS earthquake rate (λ) – also called “conditional intensity” – at time t and location (x,y)
 284 is conditioned by the past seismicity history (H_t), and is given by

$$285 \quad \lambda(x, y, t | H_t) = \mu(x, y) + \sum_{i:t_i < t} g(t - t_i, x - x_i, y - y_i; M_i), \quad (9)$$

286 with $\mu(x, y)$ the time-independent Poissonian background event rate and g the kernel that includes
 287 the triggering contribution of each earthquake occurred at $t_i < t$. The triggering part is constituted
 288 of a productivity term and temporal and spatial probability distribution functions (PDFs) that we
 289 express using the standard formulation of *Ogata* (1998):

$$290 \quad g(t, x, y; M) = K_0 e^{\alpha(M - M_{cut})} \cdot c^{p-1} (t + c)^{-p} (p - 1) \cdot f(x, y | M). \quad (10)$$

291 The first term in equation (10) governs the earthquake productivity, with M_{cut} a minimum
 292 triggering magnitude, K_0 regulates the short-term aftershock production from a parent event with
 293 $M \geq M_{cut}$, and α establishes the triggering capabilities of an earthquake as a function of its
 294 magnitude. The second term is the normalized temporal distribution of triggered events including
 295 the modified Omori-Utsu law (*Utsu, 1961*) parameters. $f(x, y | M)$ is the PDF describing the spatial

296 decay of the progeny around the parent earthquake given the parent's magnitude. For the latter,
 297 we use an isotropic power law distribution (e.g. *Ogata and Zhuang, 2006; Werner et al., 2011;*
 298 *Seif et al., 2017*):

$$299 \quad f(x, y|M) = (d e^{\gamma(M-M_{cut})})^{q-1} / \pi \cdot (x^2 + y^2 + d \cdot e^{\gamma(M_i-M_{cut})})^{-q} (q-1), \quad (11)$$

300 where q describes the spatial decay of triggered earthquakes, and $d \cdot e^{\gamma(M_i-M_{cut})}$ defines the size
 301 of the aftershock zone as a function of the parent event's magnitude (M_i).

302 We estimate the ETAS parameters (Table S1) in the testing region by means of the
 303 Maximum Likelihood Estimation (MLE) method (*Zhuang et al., 2012*) applied to the 1983-2019
 304 subset of the learning phase catalog. We use the first two years of the learning phase (1981-1982)
 305 as auxiliary seismicity to account for event interactions outside the target time window. The fitting
 306 process also considers earthquake triggering coming from outside the spatial boundaries of the
 307 target region by including the contribution of the M2.5+ seismicity occurred within the entire
 308 Southern California Seismic Network (SCSN) authoritative region. We set $M_{cut} = 2.5$ and $\alpha =$
 309 $\beta = \log(10) \cdot b$ (with Gutenberg-Richter b -value = 1) to improve ETAS' productivity forecasts
 310 (*Hainzl et al., 2008; Seif et al., 2017; Zhang et al., 2020*). We keep the ETAS parameters fixed
 311 during the whole 1-month horizon and simulate 1,000 catalogs in each forecast time window (dt).

312

313 **Results**

314 Here, we present (1) the stress interaction results considering the UCERF3 faults within a
 315 ~120 km radius from the mainshocks and (2) the physics-based and statistical forecasts expressed
 316 as expected number of events in the whole testing region within 1-day time intervals for a 1-month
 317 time horizon.

318

319 **Coulomb Stress interactions**

320 As a first order picture of coseismic stress perturbations, we estimate Coulomb stress change
321 values on (1) the surfaces of UCERF3 (*Dawson, 2013*) mapped faults and (2) on the Mw 7.1 fault
322 plane using the geometry reported in the USGS finite-fault model. For these calculations, we
323 implement a slightly coarser discretization considering 5-km depth intervals between 0-25 km
324 (Figure 2) and a wide range of friction coefficients (0.2-0.8). The 4 July Mw 6.4 earthquake
325 moment tensor calculation has northwest trending right-lateral, and northeast trending left-lateral
326 solutions. We choose to simulate the left-lateral plane based on observed deformation from InSAR
327 (Figure S1). We conclude that the 4 July Mw 6.4 shock likely triggered the 6 July Mw 7.1
328 earthquake based on calculated 0.08 to 0.2 MPa stress increases in the area of the Mw 7.1
329 hypocenter (Figure 2a), with the range depending on assigned friction coefficients. While failure
330 stress at the hypocentral area of the Mw 7.1 shock was increased, the eventual rupture areas around
331 that region had calculated stress decreases between -0.09 to -0.25MPa (Figure 2a). It does not
332 appear that the Mw 7.1 slip distribution was affected by these stress decreases because it shows
333 relatively uniform slip despite the stress change variations (Figure S2). The 4 July Mw 6.4
334 generally reduced stress or caused very small increases on most nearby surrounding faults (as
335 defined by UCERF3) with the exception of the central Garlock fault, which had a more significant
336 stress increase of 0.03 to 0.07 MPa (Figure 2a).

337 The combined stress change effects of the 4 July Mw 6.4 and 6 July Mw 7.1 earthquakes are
338 calculated on surrounding UCERF3 faults (Figure 2b). The Garlock fault is the longest fault in the
339 region and is believed by some to have the potential to host the largest earthquakes; the central
340 segment of this fault had a maximum 0.006-0.338 MPa stress increase caused by the combined
341 Mw 6.4 and Mw 7.1 Ridgecrest earthquakes. Significant ($\Delta CFF \geq 0.01\text{MPa}$; *Harris and Simpson,*

342 1992; *Hardebeck et al.*, 1998) stress increases are also noted on the Southern Sierra Nevada Fault
343 (maximum $\Delta\text{CFF} = 0.258$ MPa), Owens Valley (0.116 MPa), Tank Canyon (0.090 MPa),
344 Panamint Valley faults (0.048 MPa), Lake Isabella (0.042 MPa) and Blackwater (0.036 MPa)
345 (Table S2).

346

347 **Earthquake Forecasts**

348 Here, we present the results in terms of (a) time evolution of expected seismicity, (b) spatial
349 maps of M2.5+ expected earthquakes within specific time periods starting after the Mw 6.4 Searles
350 Valley event, for the short (24 hours after the mainshocks), and intermediate-term (1 month) time
351 windows. We also present the model validation for the first month of the Ridgecrest sequence
352 using the S and T-test metrics (*Zechar et al.*, 2010; *Rhoades et al.*, 2011) implemented in the CSEP
353 initiative, which perform a model-data consistency check and an inter-model predictive skill
354 comparison, respectively. All forecast model results are provided in the electronic supplement to
355 this article (Figures S3-S6).

356

357 ***Earthquake Rates Forecast***

358 In Figure 3a we present the M2.5+ observed vs. expected daily occurrences. The preliminary
359 and oversimplified CRS1-*basic* underestimates the seismicity rates by an order of magnitude,
360 which is in agreement with the results from a similar stress-based implementation in other
361 sequences (e.g. *Mancini et al.*, 2019). We observe that the introduction of optimized fault
362 constitutive parameters in CRS2-*optimized* reverses the severe under-prediction of CRS1-*basic*,
363 making all the successive realizations comparable to the real-time catalog. While we find that all
364 the physics-based models match well with the number of M2.5+ events in the 24 hours following

365 the Mw 6.4 event, they mostly overpredict in the short-term after the Mw 7.1 shock, for a
366 maximum of 120% in CRS2 (1579 M2.5+ expected vs. 713 observed) and a minimum of 26% in
367 CRS7 (899 expected events), with a general good agreement over the entire first month of the
368 sequence. The ETAS model, with rates expressed from the mean of the simulations, strongly
369 overpredicts after both mainshocks. However, we expect the early incompleteness of the real-time
370 catalog following the Ridgecrest main events to affect the apparent overprediction of most of the
371 models.

372 Figure 3b compares the cumulative number of expected vs. observed earthquakes. We find that
373 (1) the inclusion of secondary triggering effects from CRS4-*secondary* onwards leads to a 15%
374 increase in the cumulative number of forecasted aftershocks during the first month, almost entirely
375 due to the short-term triggering expected from the early Mw 7.1 aftershocks (days 2-3); (2) CRS6-
376 *eFFM*, based on the edited USGS finite-fault model (*eFFM*), reduces the 24 hours post-mainshock
377 over-prediction; (3) the update of the receivers using the unfolding aftershock rupture parameters
378 (CRS7-*new_FMs*), although appearing not critical immediately after the Ridgecrest mainshock
379 (<1 day) due to the limited number of available early focal mechanisms, brings an important
380 improvement between days 2 and 3 by reducing the overprediction seen in models CRS4/5/6; (4)
381 although ETAS fits the seismicity decay well in the 34-hour window between the main events, it
382 presents the poorest performance immediately after the Mw 7.1 shock; (5) stress-based models fit
383 adequately the seismicity decay from the third day onwards, with model CRS7-*new_FMs* better
384 approximating the total number of events within Poissonian uncertainty.

385 We finally test how the implementation of a different coefficient of friction in the Coulomb
386 calculations affects the output of the best performing model. When we use μ' values of 0.2 and
387 0.6, we find a variability of the expected rates after the mainshocks of about $\pm 20\%$ (Figure S3),

388 which reflects the importance of coseismic normal stress changes. Here, we consider a spatially
389 uniform coefficient of friction, such that varying its value does not affect the spatial performance
390 of the forecast. However, the array of faults in the region likely have different apparent friction
391 coefficients, with small, limited offset faults having higher values than more evolved higher slip
392 faults (e.g., *Parsons et al.*, 1999). In an operational forecast setting where it is not possible to assess
393 the frictional state of every fault, an average intermediate value is a reasonable approach for a
394 broad region.

395

396 ***Forecast Maps***

397 Figure 4 shows the seismicity rate maps of the most preliminary (CRS1-*basic*) and the most
398 enhanced (CRS7-*new_FMs*) physics-based forecasts against the statistical ETAS realization for
399 the 24 hours following the Mw 6.4 Searles Valley and the Mw 7.1 Ridgecrest events and for the
400 whole 1-month horizon. Although we formally assess the performance of the models for the entire
401 testing area, in Figure 4 we show the sub-region characterized by the highest aftershock
402 productivity. Similar maps for the complete set of models, including the alternative CRS7-*usgs*,
403 are available as supplemental material to this paper (Figures S4-S6).

404 The expected CRS and ETAS seismicity patterns in the 24 hours following the Mw 6.4 Searles
405 Valley event (Figure S4) mostly miss the observed L-shaped aftershock distribution. The visual
406 comparison between the stress-based models (Figures 4a,d and S4a-h) and ETAS (Figure 4g)
407 shows how both forecasting methods suffer from the lack of a finite-fault model that describes the
408 complex slip distribution along either the NE-SW left-lateral or NW-SE right-lateral fault sections
409 involved. The most striking feature of these maps is the misalignment between the expected vs.
410 observed seismicity along the left-lateral fault (Figure 4a), arising from the selection of the

411 kinematic parameters assigned to the Mw 6.4 rupture. For the CRS models, including CRS6-
412 *eFFM*, we initially use the real-time catalog of focal mechanisms by the SCEDC where a strike =
413 69° was reported. However, the USGS strike of 48° better matches visually the distribution of
414 triggered aftershocks along the Mw 6.4 left-lateral and also part of the right-lateral rupture before
415 the Mw 7.1 event (CRS7-*usgs*, Figure S4h). This result highlights the critical role of real-time
416 rupture characterization for operational earthquake forecasting purposes, especially since the
417 uncertainties behind fault strike angles in modern networks reach 20° (Kagan, 2003). Figure S4
418 shows that this misalignment only partially recovers when rates are enhanced by the
419 implementation of optimized rate-and-state variables (CRS2; Figure S4b) and off-fault receiver
420 planes are based on regional faulting styles (CRS3; Figure S4c). The lack of M2.5+ seismicity in
421 the real-time ComCat catalog in the 31 minutes between the Mw 4.0 foreshock and the Mw 6.4
422 Searles Valley earthquake results in minimal differences in the spatial distribution of expected
423 rates between CRS3 and the remaining stress-based models.

424 The forecast maps for the first 24 hours after the Mw 7.1 Ridgecrest mainshock (Figure S5)
425 show that: (1) the highly clustered seismicity at the northwestern fault edge is captured even in the
426 preliminary CRS1-*basic* model, although the uniform slip model results in misaligned aftershock
427 distributions (Figure 4b); (2) from CRS2 onwards, seismicity rates increase across the Ridgecrest
428 fault, marking the importance of an optimized rate-and-state parameterization; (3) the finite-fault
429 slip model incorporation leads to high near-source rates in agreement with the distribution of early
430 aftershocks (CRS3, Figure S5c) but also increased rates east of the South Sierra Nevada Fault: the
431 latter likely are an artifact due to the noisy preliminary USGS source model; (4) the early post-
432 mainshock seismicity NW of the Coso Volcanic Field (CVF) is partially underestimated initially
433 (Figure S5, c-d) but recovers when coseismic stresses are resolved on pre-existing ruptures taken

434 from past focal mechanisms (Fig S5e); (5) the edited USGS finite-fault slip model improves the
435 expected patterns east of the South Sierra Nevada Fault and reduces the overestimation in the
436 southern CVF region; (6) the isotropic ETAS model adequately captures the triggered seismicity
437 in the near source, but overpredicts in the off-fault region and underestimates observed rates
438 northwest of the CVF (Figure 4h).

439 The 1-month cumulative maps (Figure S6) illustrate that: (1) the preliminary model suffers
440 from underestimation within stress shadows and the previously described misalignment resulting
441 from the use of the SCEDC preliminary focal mechanism (Figure 4c); (2) the near-source forecast
442 improves when using the finite-fault slip model though in its preliminary non-edited version
443 (CRS3-*FFM/SSI*, Figure S6c) while the visual comparison suggests further local improvements
444 when secondary triggering effects are considered (CRS4-*secondary*, Figure S6d); (3) the small-
445 scale rupture heterogeneity, represented by pre-existing ruptures taken from past focal
446 mechanisms, provides benefits to the off-fault representation (CRS3 vs. CRS5, Figure S6c,e); (4)
447 updating the receiver fault representation to include evolving aftershock planes presents localized
448 differences in expected rates that become also notable on the SE fault termination near the central
449 Garlock Fault (Figure 4f); (5) the ETAS model (Figure 4i) accurately reproduces the high observed
450 rates in the near-source area and around the CVF but, given its basic parameterization that does
451 not incorporate fault information, it projects too wide an aftershock zone that leads to
452 overprediction at intermediate distances.

453 The most advanced CRS7-*new_FMs* model predicts heightened rates on the northern section of
454 South Sierra Nevada (SSN), and less heightened rates on southern Garlock, around the southern
455 Owens Valley, Lake Isabella and White Wolf faults (Figure S7a). We do not predict important
456 triggered seismicity on the Panamint Valley Fault, Tank Canyon and on the southern SSN section.

457 A common output from all the physics-based forecast models is the increased expected rate along
 458 the Central Garlock Fault which is yet to be observed as of the time of writing.

459

460 **Statistical Evaluation of Model Performance**

461 We quantify the predictive skills of the models by means of two statistical tests currently
 462 implemented by the Collaboratory for the Study of Earthquake Predictability. To assess the
 463 absolute spatial performance of the forecasts, we use the S-test joint log-likelihood scores (jLL_S ;
 464 *Zechar et al.*, 2010) for the 24 hours following the two mainshocks and for the 1-month cumulative
 465 forecast horizon. We then carry out a comparative analysis of model performance through the T-
 466 test metrics (*Rhoades et al.*, 2011) describing the information gains per earthquake (IG) with
 467 respect to the simple model CRS1-*basic*. Table 2 summarizes the statistical scores of the physics-
 468 based and ETAS models.

469 We compare the ability of models to reproduce the spatial aftershock patterns by expressing
 470 the forecasts in term of cumulative joint log-likelihood vs. time over the entire testing region.
 471 Given a forecast λ , we calculate the logarithm of the likelihood (LL) of observing ω earthquakes
 472 at each 2x2 km cell of the domain as (*Schorlemmer et al.*, 2007):

473

$$474 \quad LL(\omega|\lambda) = \log(Pr(\omega|\lambda)) = -\lambda + \omega \log \lambda - \log(\omega!), \quad (12)$$

475

476 where $Pr(\omega|\lambda)$ is the probability of observing ω assuming that λ is correct. The log-likelihoods
 477 used in the S-test (LL_S) make use of normalized λ rates in order to isolate the spatial component
 478 of the forecasts. By simply summing the LL_S of all the (i, j) cells, we obtain the joint S-test log-
 479 likelihood scores (jLL_S):

$$jLL_S(\Omega|\Lambda) = \sum_{(i,j) \in R} \left(-\lambda(i,j) + \omega(i,j) \log(\lambda(i,j)) - \log(\omega(i,j)!) \right), \quad (13)$$

480
481
482 where Ω and Λ are the observed and forecasted catalogs. Log-likelihoods are negative by
483 definition, with higher values indicating better predictive skills. Figure 5 shows the cumulative
484 temporal evolution of jLL_S . We find that: (1) ETAS and the most enhanced CRS7 achieve the best
485 overall spatial consistency; (2) CRS7-*usgs* presents similar spatial performance to ETAS within
486 the first week of the sequence, with the Mw 6.4 USGS focal mechanism implementation increasing
487 significantly its likelihood score (in the first 24 hours of the experiment, CRS7-*usgs*_{JLLS} = -599 vs.
488 ETAS_{JLLS} = -361); (3) stress-based forecasts from CRS5-*past_FMs* onwards outperform the
489 isotropic ETAS model after the Ridgecrest mainshock (Table 2), underscoring the importance of
490 updating the receiver plane representation using past (CRS5) or both past and aftershock focal
491 mechanism planes (CRS7-*new_FMs*); (4) the systematic log-likelihood increase with the growing
492 CRS model complexity illustrates how different components (e.g. the Mw 7.1 slip model,
493 secondary triggering effects, receiver updates) improve the overall model performance.
494 We also find that the implementation of a reference seismicity rate in CRS7-*new_FMs* improves
495 the joint log-likelihood in the 24 hours after the Mw 6.4 event (Figure 7c). However, the score
496 deteriorates following the Mw 7.1 mainshock reaching a slightly worse performance in the
497 intermediate term when compared to the model version implementing a background rate. This
498 result is due to the higher rates projected by the model in zones of high clustering of past triggered
499 seismicity, such as the area of the 1995 Ridgecrest aftershock sequence and the regions within and
500 NE of the Coso field (Figure 7d); in the latter three regions, no significant clustering of M2.5+
501 aftershocks was observed during the first month of the 2019 sequence.

502 We rank the relative forecast performance using the T-test and information gain (IG)
 503 metrics, defined as the average log-likelihood difference per earthquake between a model (A) and
 504 a benchmark (B):

$$505 \quad IG(A, B) = \frac{jLL_A - jLL_B}{N}, \quad (14)$$

506
 507 where N is the number of observed events. T-test's likelihoods are calculated from unnormalized
 508 rates so that both the spatial aftershock distribution and the forecasted seismicity rates influence
 509 the score. We calculate the 95% confidence interval over the mean IG from a paired Student's t-
 510 test (*Rhoades et al.*, 2011). A positive information gain per earthquake presents an improvement
 511 with respect to a benchmark, and we deem the improvement significant if the confidence interval
 512 does not enclose zero. In Figure 6 we compare the average daily information gains when CRS1-
 513 *basic* is taken as benchmark. The short-term results for the 24 hours after the Mw 6.4 suggest that
 514 although all physics-based models are genuinely more informative than CRS1 ($IG_{CRS-1} \geq 2.5$) none
 515 of them except the most enhanced one (CRS7-*usgs*, $IG_{CRS1} = 5.65 \pm 0.49$; grey square in Figure
 516 6a) perform as well as ETAS ($IG_{CRS1} = 6.40 \pm 0.41$). Following the Mw 7.1 Ridgecrest mainshock
 517 (Figure 6b) ETAS is outperformed by most of the stress-based forecasts as shown by the low IG
 518 values. Here, the decisive factors behind the CRS performance improvement are the edited fault
 519 slip model and the receiver updates. We also find a small overall performance improvement (ΔIG
 520 ≈ 0.15) when receiver planes are updated using the first 34 hours aftershocks (CRS7-*new_FMs*);
 521 rupture parameters for this time window are taken from the admittedly limited number of early
 522 aftershock focal mechanisms but, as we show further on, this improvement presents a significant
 523 spatial component. The cumulative 1-month evaluation window (Figure 6c) reveals similar
 524 information gain patterns. Here, CRS7-*new_FMs* outperforms CRS5-*past_FMs* highlighting the

525 medium-term effect of receiver plane updates within the evolving sequence. Finally, the enhanced
526 physics-based model CRS7-*usgs* achieves a higher mean average information gain per earthquake
527 than ETAS.

528 By plotting the log-likelihood differences in the space domain (Figure S8), we observe that
529 the fault-based CRS forecasts are more localized along the ruptures when compared to the standard
530 ETAS model and outperform the statistical counterpart in the broader region by predicting low
531 off-fault rates (Figure S8b). However, if we look at smaller distances, we notice that the ETAS
532 model is more robust on the strictly near-fault area (Figure S8c) in agreement with similar previous
533 experiments (e.g. *Segou et al.*, 2013; *Mancini et al.*, 2019), although the enhanced physics-based
534 model CRS7-*usgs* significantly outperforms ETAS in the region of high aftershock clustering
535 around the north-western edge of the Ridgecrest rupture.

536 To better evaluate the effect of updating the receiver planes during the unfolding aftershock
537 sequence, we show in Figure 7a the T-test's log-likelihood differences for the 1-month forecast
538 between CRS6, updated by past focal mechanisms, and CRS7, updated by past and evolving focal
539 mechanisms. We see two regions characterized by a clear performance improvement (green cells)
540 arising within an otherwise noisy ΔLL signal. We exclude from this discussion the wider area of
541 the Coso field since triggering mechanisms within this active volcanic region may be influenced
542 by other phenomena (e.g. fluid flow; *Martinez-Garzón et al.*, 2018). In Figure 7b-d, we plot the
543 distributions of pre- and post-Ridgecrest focal mechanisms in the identified regions using the
544 ternary diagrams of *Frohlich and Apperson* (1992), with the addition of a third zone of interest
545 close to the Garlock Fault characterized by lower aftershock rates and mostly unvaried CRS model
546 performance. To facilitate our interpretation, we present focal mechanisms of cells with notable
547 cumulative log-likelihood difference $|\Delta LL| \geq 6$. In the southern-edge zone, the significance behind

548 the update using evolving focal mechanisms (Figure 7d) is smaller since the pre- and post-
549 Ridgecrest focal mechanism populations remains similar. However, the results suggest a shift
550 between pre- and post-Ridgecrest focal mechanism distributions in the two areas (Zone 1 and 2;
551 Figure 7b-c) where the receivers update with evolving aftershocks leads to a robust improvement,
552 with promoted strike-slip ruptures (from 54% to 69% and from 53% to 67% in zones 1 and 2,
553 respectively) and suppressed normal fault aftershocks (from 25% to 10% and from 24% to 13%).
554 To determine whether the pre-existing normal faulting (pre-Ridgecrest) is in fact discouraged
555 within the evolving sequence, we resolve the Ridgecrest coseismic stress changes on the average
556 plane of the pre-Ridgecrest normal focal mechanisms (Figure S9). Indeed, we find that the ΔCFF
557 estimates support a near source stress shadow on pre-existing normal faults that is more evident
558 between 2-12 km depth in Zone 2 (Figure S9, b-f) and below 4 km in Zone 1 (Figure S9 c-f). The
559 latter observation provides a physical basis for the shift in the focal mechanism population during
560 the unfolding Ridgecrest sequence but also points out the importance of forecast updates using
561 aftershock data.

562

563 **Discussion and Conclusions**

564 We tested the predictive skills of seven Coulomb rate-and-state (CRS) forecasts developed
565 within a pseudo-prospective experiment covering the first month of the 2019 Ridgecrest sequence.
566 Our models progressively evolve in their implementation: from an over-simplified
567 parameterization, based on uniform slip representation and parallel receiver faults, to the most
568 complex physical model incorporating optimized rate-and-state fault constitutive parameters,
569 secondary triggering effects, the USGS Mw 7.1 finite-fault slip model and receivers that consider
570 the UCERF3 faults, off-fault rupture patterns based on pre-existing ruptures, and finally near-

571 source rupture planes revealed by unfolding aftershocks. The forecast results suggest high
572 expected rates along the whole ~75 km long near-fault region, as confirmed by the observed
573 events. All physics-based models expect increased seismicity rates in Central Garlock Fault,
574 though not significant reactivation has occurred at the time of this writing other than the observed
575 triggered creep (*Barnhart et al.*, 2019). However, delayed aftershocks may be expected on low-
576 stressing rate faults, which highlights the challenges that short- and long-term forecasts must
577 address (*Toda and Stein*, 2018).

578 When we validate models by means of the formal statistical tests currently implemented
579 within the CSEP community (*Zechar et al.*, 2010; *Rhoades et al.*, 2011), we see that our results
580 agree with recent works suggesting that advances in the implementation of short-term physics-
581 based earthquake forecasting (e.g. *Segou and Parsons*, 2016) show significant performance
582 increases and can approach, or at times outperform, simple benchmark ETAS models. Specifically,
583 our results confirm those of previous forecast experiments suggesting that critical components
584 such as finite-fault rupture models, secondary triggering effects, optimized rate-and-state
585 parameters and spatially variable receiver faults significantly enhance the predictive skills of
586 Coulomb stress-based models (*Cattania et al.*, 2018; *Mancini et al.*, 2019). Our conclusions are
587 further supported by recent modelling developments that illustrate the importance of past focal
588 mechanism data in the estimation of aftershock rupture styles (*Segou and Parsons*, 2020).

589 Importantly, in this study we evaluated the significance of updating critical components of
590 physics-based models, such as the receiver planes, using aftershock data from the unfolding
591 Ridgecrest sequence. The observed evolving spatial and temporal diversity between the pre-
592 Ridgecrest and within-sequence focal mechanism populations offers a physical interpretation for
593 the estimated local performance improvement, reflected in higher information gains in different

594 regions across the fault. We document a shift in the faulting styles of local triggered seismicity
595 illustrated by a decrease in the percentage of normal fault earthquakes (~25% pre-Ridgecrest vs.
596 ~10% within the aftershock sequence). In that context, earthquakes on specific pre-existing
597 faulting styles at a local fine scale might be suppressed while others may be enhanced. Therefore,
598 updating the modelled source and receiver populations as aftershock data unfolds is an important
599 step for improving the performance of short-term stress-based earthquake forecasts.

600 On the other hand, our experimental design showcases one of the modelling caveats that
601 currently affect physics-based aftershock forecasts. We clearly see how, even in a data-rich
602 environment for real-time earthquake products such as California, uncertainties of early focal
603 mechanisms and slip models can be detrimental for operational stress-based forecast models. In
604 particular, the variability of the kinematic parameters associated to the Mw 6.4 Searles Valley
605 event from different providers reveals the influence of data choices among multiple authoritative
606 sources. However, it is extremely encouraging that, although subject to assumptions regarding
607 epistemic and aleatory uncertainties, the most enhanced CRS models that make use of aftershock
608 data can generate informative forecasts that are beginning to compare well to those of statistical
609 models.

610

611 **Data and resources**

612 Some data used in this study were collected by the California Institute of Technology
613 (Caltech) and U.S. Geological Survey (USGS) Southern California Seismic Network
614 (<https://doi:10.7914/SN/CI>) and distributed by the Southern California Earthquake Data Center
615 (SCEDC). The *Hauksson et al. (2012)* and *Yang et al. (2012)* catalogs of seismicity and focal
616 mechanisms can be acquired through access to the SCEDC website

617 (<https://scedc.caltech.edu/research-tools/altcatalogs.html>), as well as the catalog of focal
618 mechanisms for the Ridgecrest sequence ([https://service.scedc.caltech.edu/eq-](https://service.scedc.caltech.edu/eq-catalogs/FMsearch.php)
619 [catalogs/FMsearch.php](https://service.scedc.caltech.edu/eq-catalogs/FMsearch.php)). The ANSS Comprehensive Earthquake Catalog (ComCat) can be
620 searched at <https://earthquake.usgs.gov/earthquakes/search/>. The stress inversion by *Luttrell and*
621 *Smith-Konter* (2017) is available on the SCEC Community Stress Model webpage
622 (<https://www.scec.org/research/csm>). The preliminary slip model by G. P. Hayes (USGS) for the
623 Mw 7.1 Ridgecrest mainshock is available at the USGS event webpage:
624 <https://earthquake.usgs.gov/earthquakes/eventpage/ci38457511/finite-fault>. UCERF3 fault
625 section data is accessible through the open-file report at
626 http://pubs.usgs.gov/of/2013/1165/pdf/ofr2013-1165_appendixC.pdf.
627 The code ‘CRS’ (*Cattania and Khalid*, 2016) can be downloaded at <https://github.com/camcat/crs>.
628 Coseismic stress change on 3D individual UCERF3 faults are calculated using Coulomb 3.3 (*Toda*
629 *et al.*, 2011; <https://earthquake.usgs.gov/research/software/coulomb/>) and the software ‘DLC’ by
630 R. Simpson (USGS) based on the subroutines of *Okada* (1992). The supplemental material
631 attached to this manuscript provides the full set of forecast maps, model testing results, and static
632 stress changes calculations.

633

634 **Acknowledgments**

635 The authors would like to thank the Editor-in-Chief Thomas Pratt, the Guest Editor
636 Zachary E. Ross and two anonymous reviewers for the thorough and insightful comments that
637 helped us improving the manuscript.

638 S. Mancini is supported by a NERC GW4+ Doctoral Training Partnership studentship from
639 the Natural Environment Research Council (NE/L002434/1) and by the BGS University Funding

640 Initiative Ph.D. studentship (S350). This project (M.J.W.) has received funding from the European
641 Union's Horizon 2020 research and innovation program under grant agreement No 821115, Real-
642 Time Earthquake Risk Reduction for a Resilient Europe (RISE) and (M.S.) from the NERC-
643 NSFGE0 funded project 'The Central Apennines Earthquake Cascade Under a New Microscope'
644 (NE/R0000794/1). This research was also supported by the Southern California Earthquake Center
645 (Contribution No. 10017). SCEC is funded by NSF Cooperative Agreement EAR-1600087 &
646 USGS Cooperative Agreement G17AC00047.

647

648 **References**

649

650 Barnhart, W. D., G. P. Hayes, and R. D. Gold (2019). The July 2019 Ridgecrest, California,
651 earthquake sequence: Kinematics of slip and stressing in cross-fault ruptures, *Geophys. Res.*
652 *Lett.* 46. <https://doi.org/10.1029/2019GL084741>

653 Bryant, W.A., compiler, 2017, Fault number 72, Little Lake fault zone, in Quaternary fault and
654 fold database of the United States: U.S. Geological Survey website,
655 <https://earthquakes.usgs.gov/hazards/qfaults>

656 Cattania, C., and F. Khalid (2016). A parallel code to calculate rate-state seismicity evolution
657 induced by time dependent, heterogeneous Coulomb stress changes, *Computers & Geosciences*
658 94, 48-55.

659 Cattania, C., M. J. Werner, W. Marzocchi, S. Hainzl, D. Rhoades, M. Gerstenberger, M. Liukis,
660 W. Savran, A. Christophersen, A. Helmstetter, A. Jimenez et al. (2018). The Forecasting Skill
661 of Physics-Based Seismicity Models during the 2010–2012 Canterbury, New Zealand,
662 Earthquake Sequence. *Seismol. Res. Lett.* 89(4), 1238–1250.
663 <https://doi.org/10.1785/0220180033>.

- 664 Chen, K. H., R. Bürgmann, and R. M. M. Nadeau (2013). Do earthquakes talk to each other?
665 Triggering and interaction of repeating sequences at Parkfield, *J. Geophys. Res. Solid Earth*
666 118, 165–182, <https://doi.org/10.1029/2012JB009486>.
- 667 Chen, K., J. Avouac, S. Aati, C. Milliner, F. Zheng, and C. Shi (2020). Cascading and pulse-like
668 ruptures during the 2019 Ridgecrest earthquakes in the Eastern California Shear Zone, *Nat.*
669 *Comm.* 11, 22. <https://doi.org/10.1038/s41467-019-13750-w>.
- 670 Dawson, T. E. (2013). Appendix A – Updates to the California Reference Fault Parameter
671 Database – Uniform California Earthquake Rupture Forecast, Version 3 Fault Models 3.1 and
672 3.2, U.S. Geological Survey Open-File Report, 2013–1165, 18 p.,
673 http://pubs.usgs.gov/of/2013/1165/pdf/ofr2013-1165_appendixC.pdf
- 674 Dieterich, J. H. (1994). A constitutive law for rate of earthquake production and its application to
675 earthquake clustering, *J. Geophys. Res.*, 99(B2), 2601–2618.
- 676 Dieterich, J. H., V. Cayol, and P. Okubo (2000). The use of earthquake rate changes as stress meter
677 at Kilauea volcano, *Nature.*, 408, 457–460.
- 678 Field, E. H., K. R. Milner, J. L. Hardebeck, M. T. Page, N. van der Elst, T. H. Jordan, A. J. Michael,
679 B. E. Shaw, and M. J. Werner (2017). A spatiotemporal clustering model for the third Uniform
680 California Earthquake Rupture Forecast (UCERF3-ETAS): toward an operational earthquake
681 forecast, *Bull. Seismol. Soc. Am.* 107(3), 1049-1081. <https://doi.org/10.1785/0120160173>.
- 682 Frohlich, C., and K. Apperson (1992). Earthquake focal mechanisms, moment tensors, and the
683 consistency of seismic activity near plate boundaries, *Tectonics* 11(2), 279-296.
- 684 Gerstenberger, M. C., and D. A. Rhoades (2010). New Zealand earthquake forecast testing centre,
685 *Pure Appl. Geophys.* 167, 8-9. 877-892. <https://doi.org/10.1007/s00024-010-0082-4>.
- 686 Guy, M., J. Patton, J. Fee, M. Hearne, E. Martinez, D. Ketchum. C. Worden, V. Quitariano, E.
687 Hunter, G. Smoczyk et al. (2015). National Earthquake Information Center systems overview
688 and integration (USGS numbered series No. 2015–1120), Open-File Report. U.S. Geological
689 Survey, Reston, VA.

- 690 Hainzl, S., A. Christophersen, and B. Enescu (2008). Impact of earthquake rupture extension on
691 parameters estimations of point-process models, *Bull. Seismol. Soc. Am.* 98(4), 2066-2072.
692 <https://doi.org/10.1785/0120070256>.
- 693 Hainzl, S., O. Zakharova, and D. Marsan (2013). Impact of aseismic transients on the estimation
694 of aftershock productivity parameters, *Bull. Seismol. Soc. Am.* 103, 1723–1732.
- 695 Hanks, T., and H. Kanamori (1979). A moment magnitude scale, *J. Geophys. Res.* 84, 2348–2350.
696 <https://doi.org/10.1029/JB084iB05p02348>.
- 697 Hardebeck, J. L., J. J. Nazareth, and E. Hauksson (1998). The static stress change triggering model:
698 Constraints from two southern California earthquake sequences, *J. Geophys. Res.*, 103, 24427-
699 24437.
- 700 Harris, R. A., and R. W. Simpson (1992). Changes in static stress on southern California faults
701 after the 1992 Landers earthquake, *Nature* 360(6401), 251–254.
- 702 Hauksson, E., K. Hutton, H. Kanamori, L. Jones, J. Mori, S. E. Hough, and G. Roquemore (1995).
703 Preliminary report on the 1995 Ridgecrest earthquake sequence in Eastern California, *Seismol.*
704 *Res. Lett.*, 66(6), 54-60.
- 705 Hauksson, E., W. Yang, and P. M. Shearer (2012). Waveform relocated earthquake catalog for
706 southern California (1981 to 2011). *Bull. Seismol. Soc. Am.* 102(5), 2,239–2,244.
- 707 Heimisson, E. R., and P. Segall (2018). Constitutive law for earthquake production based on rate-
708 and- state friction: Dieterich 1994 revisited. *J. Geophys. Res. Solid Earth* 123, 4141- 4156.
709 <https://doi.org/10.1029/2018JB015656>.
- 710 Heimisson, E. R. (2019). Constitutive law for earthquake production based on rate-and- state
711 friction: Theory and Application of Interacting Sources. *J. Geophys. Res. Solid Earth* 124,
712 1802- 1821. <https://doi.org/10.1029/2018JB016823>.
- 713 Helmstetter, A., Y. Y. Kagan, and D. D. Jackson (2005). Importance of small earthquakes for
714 stress transfers and earthquake triggering, *J. Geophys. Res.* 110.
715 <https://doi.org/10.1029/2004JB003286>.

- 716 Helmstetter, A., Y. Kagan, and D. D. Jackson (2006). Comparison of short-term and time-
717 independent earthquake forecast models for Southern California, *Bull. Seismol. Soc. Am.* 96(1),
718 90–106. <https://doi.org/10.1785/0120050067>.
- 719 Helmstetter, A., Kagan, Y., & Jackson, D. D. (2007). High-resolution Time-independent Grid-
720 based Forecast for $M \geq 5$ Earthquakes in California. *Seismol. Res. Lett.*, 78(1), 78-86.
721 <https://doi.org/10.1785/gssrl.78.1.78>.
- 722 Jordan, T. H. (2006). Earthquake Predictability, Brick by Brick, *Seismol. Res. Lett.* 77(1), 3–6.
723 <https://doi.org/10.1785/gssrl.77.1.3>.
- 724 Jordan, T. H., Y. Chen, and I. Main (2011). Operational earthquake forecasting: State of
725 knowledge and guidelines for utilization, *Ann. Geophys.* 54, no. 4. [https://doi.org/10.4401/ag-](https://doi.org/10.4401/ag-5350)
726 [5350](https://doi.org/10.4401/ag-5350).
- 727 Jordan, T. H., W. Marzocchi, A. J. Michael, and M. C. Gerstenberger (2014). Operational
728 Earthquake Forecasting Can Enhance Earthquake Preparedness, *Seismol. Res. Lett.* 85(5), 955–
729 959. <https://doi.org/10.1785/0220140143>.
- 730 Kagan, Y. Y. (2003). Accuracy of modern global earthquake catalogs, *Phys. Earth Planet. In.* 135,
731 173–209.
- 732 Linker, M. F., and J. H. Dieterich (1992). Effects of variable normal stress on rock friction:
733 Observations and constitutive equations, *J. Geophys. Res.*, 97(92), 4923-4940.
734 <https://doi.org/10.1029/92JB00017>
- 735 Luttrell, K., and B. Smith-Konter (2017). Limits on crustal differential stress in southern California
736 from topography and earthquake focal mechanisms, *Geophys. J. Int.* 211, 472–482.
737 <https://doi.org/10.1093/gji/ggx301>.
- 738 Mancini, S., M. Segou, M. J. Werner, and C. Cattania (2019). Improving physics-based aftershock
739 forecasts during the 2016-2017 Central Italy earthquake cascade, *J. Geophys. Res. Solid Earth*
740 124. <https://doi.org/10.1029/2019JB017874>.

- 741 Martinez-Garzón, P., I. Zaliapin, Y. Ben-Zion, G. Kwiatek, and M. Bohnhoff (2018). Comparative
742 study of earthquake clustering in relation to hydraulic activities at geothermal fields in
743 California, *J. Geophys. Res.* 123, 4041-4062.
- 744 Marzocchi W., A. M. Lombardi, and E. Casarotti (2014). The establishment of an operational
745 earthquake forecasting system in Italy, *Seismol. Res. Lett.* 85(5), 961-969.
- 746 Michael, A. J., and M. J. Werner (2018). Preface to the Focus Section on the Collaboratory for the
747 Study of Earthquake Predictability (CSEP): New Results and Future Directions, *Seismol. Res.*
748 *Lett.* 89(4), 1226-1228. <https://doi.org/10.1785/0220180161>.
- 749 Mousavi, M., W. Zhu, Y. Sheng, and G. Beroza (2019). CRED: a deep residual network of
750 convolutional and recurrent units for earthquake signal detection, *Sci. Rep.* 9, 10267.
751 <https://doi.org/10.1038/s41598-019-45748-1>.
- 752 Okada, Y. (1992). Internal deformation due to shear and tensile faults in a half-space, *Bull.*
753 *Seismol. Soc. Am.* 82, 1018-1040.
- 754 Ogata, Y. (1988). Statistical models for earthquake occurrences and residual analysis for point
755 processes, *J. Am. Stat. Assoc.* 83(401), 9–27.
- 756 Ogata, Y. (1998). Space-time point-process models for earthquake occurrences, *Ann. Inst. Stat.*
757 *Math.* 50(2), 379–402. <https://doi.org/10.1023/A:1003403601725>.
- 758 Ogata, Y., and J. Zhuang (2006). Space-time ETAS models and an improved extension,
759 *Tectonophysics* 413(1–2), 13–23.
- 760 Omi T., Y. Ogata, K. Shiomi, B. Enescu, K. Sawazaki, and K. Aihara (2019). Implementation of
761 a real-time system for automatic aftershock forecasting in Japan, *Seismol. Res. Lett.* 90(1), 242-
762 250. <https://doi.org/10.1785/0220180213>.
- 763 Parsons, T., R. S. Stein, R. W. Simpson, and P. A. Reasenberg (1999). Stress sensitivity of fault
764 seismicity: a comparison between limited-offset oblique and major strike-slip faults, *J.*
765 *Geophys. Res.* 104, 20183-20202.

- 766 Rice, J. R. (1992). Fault stress states, pore pressure distributions, and the weakness of the San
767 Andreas Fault, in *Fault mechanics and transport properties of rocks; a festschrift in honour of*
768 *W. F. Brace*, edited by B. Evans and T. Wong, Academic Press, San Diego, CA, USA., 475-
769 503.
- 770 Rhoades, D. A., D. Schorlemmer, M. C. Gerstenberger, A. Christophersen, J. D. Zechar, and M.
771 Imoto (2011). Efficient testing of earthquake forecasting models, *Acta Geophysica* 59(4), 728–
772 747. <https://doi.org/10.2478/s11600-011-0013-5>.
- 773 Ross, Z., M. A. Meier, and E. Hauksson (2018). P wave arrival picking and first-motion polarity
774 determination with deep learning, *J. Geophys. Res. Solid Earth* 122, 5120-5129.
775 <https://doi.org/10.1029/2017JB015251>.
- 776 Ross, Z., B. Idini, Z. Jia, O. L. Stephenson, M. Zhong, Z. Wang, Z. Zhan, M. Simons, E. J. Fielding,
777 S. Yun, E. Hauksson et al. (2019). Hierarchical interlocked orthogonal faulting in the 2019
778 Ridgecrest earthquake sequence, *Science* 366, 346-351.
- 779 Schorlemmer, D., M. C. Gerstenberger, S. Wiemer, D. D. Jackson, and D. A. Rhoades (2007).
780 Earthquake likelihood model testing, *Seismol. Res. Lett.* 78(1), 17–29.
781 <https://doi.org/doi:10.1785/gssrl.78.1.17>.
- 782 Segou, M., T. Parsons, and W. Ellsworth (2013). Comparative evaluation of physics-based and
783 statistical forecasts in Northern California, *J. Geophys. Res. Solid Earth* 118, 6219–6240.
784 <https://doi.org/10.1002/2013JB010313>.
- 785 Segou, M., and T. Parsons (2016). Prospective Earthquake Forecasts at the Himalayan Front after
786 the 25 April 2015 M 7.8 Gorkha Mainshock, *Seismol. Res. Lett.* 87(4),
787 <https://doi.org/10.1785/0220150195>.
- 788 Segou, M., and T. Parsons (2020). A New Technique to Calculate Earthquake Stress Transfer and
789 to Probe the Physics of Aftershocks, *Bull. Seismol. Soc. Am.* 110(2), 863–873,
790 <https://doi.org/10.1785/0120190033>.

- 791 Seif, S., A. Mignan, J. D. Zechar, M. J. Werner, and S. Wiemer (2017). Estimating ETAS: The
792 effects of truncation, missing data, and model assumptions, *J. Geophys. Res. Solid Earth* 121,
793 449–469. <https://doi.org/10.1002/2016JB012809>.
- 794 Toda, S., R. S. Stein, K. Richards-Dinger, and B. S. Bozkurt. (2005). Forecasting the evolution of
795 seismicity in southern California: Animations built on earthquake stress transfer, *J. Geophys.*
796 *Res.* 110, B05S16, <https://doi.org/10.1029/2004JB003415>.
- 797 Toda, S., R. S. Stein, V. Sevilgen, and J. Lin (2011). Coulomb 3.3 Graphic-rich deformation and
798 stress-change software for earthquake, tectonic, and volcano research and teaching – user guide:
799 U.S. Geological Survey Open-File Report 2011-1060, 63 p.,
800 <http://pubs.usgs.gov/of/2011/1060/>.
- 801 Toda, S., and R. S. Stein (2018). Why aftershock duration matters for probabilistic seismic hazard
802 assessment, *Bull. Seismol. Soc. Am.* 108(3A), 1414–1426. <https://doi.org/10.1785/0120170270>.
- 803 Utsu, T. (1961). A statistical study on the occurrence of aftershocks, *Geophys. Mag.* 30, 521–605.
- 804 Wells, D. L., and K. J. Coppersmith (1994). New empirical relationships among magnitude,
805 rupture length, rupture width, rupture area, and surface displacement, *Bull. Seismol. Soc. Am.*
806 84, 974–1002.
- 807 Werner, M. J., A. Helmstetter, D. D. Jackson, and Y.Y. Kagan (2011), High-resolution long-term
808 and short-term earthquake forecasts for California, *Bull. Seismol. Soc. Am.* 101(4), 1630–1648.
809 <https://doi.org/doi:10.1785/01200900>.
- 810 Yang, W., E. Hauksson, and P. M. Shearer (2012). Computing a large refined catalog of focal
811 mechanisms for southern California (1981–2010): Temporal stability of the style of faulting.
812 *Bull. Seismol. Soc. Am.* 102(3), 1179–1194.
- 813 Zechar, J. D., M. C. Gerstenberger, and D. A. Rhoades (2010). Likelihood based tests for
814 evaluating space-rate-magnitude earthquake forecasts, *Bull. Seismol. Soc. Am.* 100, 1184–1195.
815 <https://doi.org/10.1785/0120090192>.

816 Zhang, L., M. J. Werner, and K. Goda (2020). Variability of ETAS Parameters in Global
817 Subduction Zones and Applications to Mainshock–Aftershock Hazard Assessment, *Bull.*
818 *Seismol. Soc. Am.* 110(1), 191–212, <https://doi.org/10.1785/0120190121>.

819 Zhuang, J., Y. Ogata, and D. Vere-Jones (2002). Stochastic declustering of space-time earthquake
820 occurrences. *J. Am. Stat. Assoc.* 97(458), 369–380.
821 <https://doi.org/10.1198/016214502760046925>.

822 Zhuang, J., D. Harte, M. J. Werner, S. Hainzl, and S. Zhou. (2012). Basic models of Seismicity:
823 Temporal Models, *Community Online Resource for Statistical Seismicity Analysis*.
824 <https://doi.org/10.5078/corssa-79905851>.

825

826 **Addresses of authors**

827 Simone Mancini (simone.mancini@bristol.ac.uk), School of Earth Sciences, University of Bristol,
828 BS8 1RL Bristol, UK

829 Margarita Segou (msegou@bgs.ac.uk), British Geological Survey, The Lyell Center, Research
830 Avenue South, EH14 4AP, Edinburgh, UK

831 Maximilian Jonas Werner (max.werner@bristol.ac.uk), School of Earth Sciences, University of
832 Bristol, BS8 1RL Bristol, UK

833 Tom Parsons (tparsons@usgs.gov), United States Geological Survey, USGS P.O. Box 158,
834 Moffett Field, CA 94035, USA

835

836

837

838

839

840

841

842 **List of Figure Captions**

843 **Figure 1.** Testing region map. Earthquakes with $M_{2.5+}$ are shown: pre-Ridgecrest (1981-2019,
 844 grey circles), post Mw 6.4 Searles Valley event (orange), post Mw 7.1 Ridgecrest mainshock (red).
 845 We report the focal mechanisms of the two mainshocks. The 1 October 1982 Indian Wells event
 846 ($M=5.2$) is indicated as a green triangle. Light blue squares represent the epicenters of the 1995-
 847 1996 Ridgecrest sequence mainshocks ($M=5.4$, 17 August 1995; $M=5.8$, 20 September 1995;
 848 $M=5.2$, 7 January 1996). The 1995 Ridgecrest sequence activated a number of normal, left and
 849 right-lateral faults. Black solid lines indicate the UCERF3 (Dawson, 2013) fault traces.

850
 851 **Figure 2.** Example of calculated combined coseismic stress changes on mapped UCERF3 faults
 852 following (a) the 4 July 2019 Mw 6.4 event and (b) both the Mw 6.4 and 6 July Mw 7.1 earthquakes
 853 near Ridgecrest, CA. Hypocenters of the Mw 6.4 and Mw 7.1 earthquakes are shown by yellow
 854 stars. Displayed stress changes were calculated using a friction coefficient of 0.4. Stress increases
 855 ($\Delta CFF \geq 0.01$ MPa) are calculated on the Central Garlock, South Sierra Nevada, Owens Valley,
 856 Tank Canyon, and Panamint Valley faults (Table S2).

857
 858 **Figure 3.** Forecast time series for physics-based and statistical models for the first month of the
 859 Ridgecrest sequence. (a) Incremental time series: black triangles indicate the observed number of
 860 $M_{2.5+}$ events, while squares represent the expected numbers. (b) Comparison between the
 861 cumulative expected vs. observed (black line) rates. The shaded areas indicate Poissonian
 862 uncertainties.

863
 864 **Figure 4.** Maps of expected seismicity rates for CRS1/7 and ETAS in the area of main aftershock
 865 productivity for the first 24 hours following the two mainshocks and for the first month of the
 866 Ridgecrest sequence. Observed events ($M_{2.5+}$) in each time window are represented as circles.
 867 The dashed-line square indicates the area of the Coso volcanic field (CVF). S = sources (minimum
 868 magnitude); Opt RS = optimized rate-and-state parameters, USD = uniform slip distribution; SUP
 869 = spatially uniform receiver planes; SVP = spatially variable planes; eFFM = edited finite-fault
 870 slip model; I = isotropic stress field. $A\sigma$ values are in MPa, $\dot{\tau}$ values are in MPa/year.

871
 872 **Figure 5.** Cumulative S-test joint log-likelihood (jLL_S) timeseries. The scores are obtained by
 873 summing the S-test log-likelihoods (LL_S) of each spatial cell and 1-day time step. The vertical
 874 dashed line marks the occurrence of the Ridgecrest mainshock.

875
 876 **Figure 6.** Average daily information gain per earthquake from the preliminary CRS1-*basic* model
 877 for: (a) 24 hour after the Mw 6.4 Searles Valley event, (b) 24 hour after the Mw 7.1 Ridgecrest
 878 mainshock and (c) for a cumulative 1-month forecast horizon. The filled grey squares indicate the
 879 information gain score of the alternative CRS7-*usgs* model. The horizontal lines mark the no-gain
 880 level.

881

882 **Figure 7.** Influence of pre-existing and evolving rupture populations in stress-based forecasts. (a)
883 Map of cumulative ΔLL for the 1-month forecast horizon between CRS6-*eFFM* and CRS7-
884 *new_FMs*. Positive (green) values indicate a better performance of CRS7-*new_FMs*. Black points
885 indicate the locations of M2.5+ aftershocks between 4 July 2019 and 4 August 2019, while white
886 stars represent the two mainshocks. Values are saturated at ± 30 to facilitate visualization. (b-d)
887 Ternary diagrams showing the distribution of focal mechanisms during the pre-sequence (1981-
888 2019, magenta circles) and post-Ridgecrest (blue crosses) time windows.

889

890 **Table 1.** Main features of CRS models.
891

Model	Stress Calculations					Rate-and-state Parameters			
	M_{\min}	Secondary Triggering	Slip Distribution	μ'	Receivers	τ_0 (1981-2019)	$A\sigma$ (MPa)	$\dot{\tau}$ (MPa/year)	LL optimization
CRS1- <i>basic</i>	6.4	No	USD	0.4	SUP	He	0.05	0.0018	No
CRS2- <i>optimized</i>	6.4	No	USD	0.4	SUP	He	0.015	0.00025	Yes
CRS3- <i>FFM/SSI</i>	6.4	No	FFM ($M \geq 7$) USD ($M \geq 6$)	0.4	SVP (UCERF3 + SSI)	He	0.02	0.00027	Yes
CRS4- <i>secondary</i>	2.5	Yes	FFM ($M \geq 7$) USD ($M \geq 2.5$) I ($M \geq 2.5$)	0.4	SVP (UCERF3 + SSI)	He	0.02	0.00027	Yes
CRS5- <i>past_FMs</i>	2.5	Yes	FFM ($M \geq 7$) USD ($M \geq 2.5$) I ($M \geq 2.5$)	0.4	SVP (UCERF3 + SSI + past FMs)	He	0.02	0.00027	Yes
CRS6- <i>eFFM</i>	2.5	Yes	eFFM ($M \geq 7$) USD ($M \geq 2.5$) I ($M \geq 2.5$)	0.4	SVP (UCERF3 + SSI + past FMs)	He	0.02	0.00027	Yes
CRS7- <i>new_FMs</i>	2.5	Yes	eFFM ($M \geq 7$) USD ($M \geq 2.5$) I ($M \geq 2.5$)	0.4	SVP (UCERF3 + SSI + updating FMs)	He	0.02	0.00027	Yes
CRS7- <i>usgs</i>	2.5	Yes	eFFM ($M \geq 7$) USGS-USD ($M \geq 2.5$) I ($M \geq 2.5$)	0.4	SVP (UCERF3 + SSI + updating FMs)	He	0.02	0.00027	Yes

892
893 M_{\min} = minimum magnitude for stress sources; FM = focal mechanism; USD = uniform slip
894 distribution; FFM = finite-fault slip model; eFFM = edited finite-fault slip model; I = isotropic
895 stress field; SUP = spatially uniform receiver planes; SVP = spatially variable planes; SSI =
896 smoothed stress inversion; He = heterogeneous.

897

898

899

900

901 **Table 2.** Summary of short-term (24 hours) and intermediate-term (1 month) model performance.
 902

Model	24 hours after Mw 6.4			24 hours after Mw 7.1			1 month (cumulative)		
	jLLs	N _{F/O}	IG _{CRS1}	jLLs	N _{F/O}	IG _{CRS1}	jLLs	N _{F/O}	IG _{CRS1}
CRS1- <i>basic</i>	-1378	0.10	-	-2905	0.27	-	-8849	0.20	-
CRS2- <i>optimized</i>	-1129	0.64	2.55	-3310	2.21	-0.42	-9451	1.46	0.28
CRS3- <i>FFM/SSI</i>	-1538	0.91	2.71	-2076	1.77	1.53	-8404	1.22	1.19
CRS4- <i>secondary</i>	-1071	0.92	2.92	-2046	1.77	1.57	-7784	1.40	1.34
CRS5- <i>past_FMs</i>	-1054	0.94	3.01	-1796	1.94	1.84	-7003	1.46	1.70
CRS6- <i>eFFM</i>	-1054	0.94	3.01	-1566	1.39	2.38	-6760	1.17	1.88
CRS7- <i>new_FMs</i>	-1054	0.94	3.01	-1482	1.26	2.55	-6440	0.94	2.25
CRS7- <i>usgs</i>	-599	0.62	5.65	-1627	1.28	3.35	-6146	0.92	2.50
ETAS	-361	1.75	6.41	-1982	2.61	1.22	-5699	1.98	2.32

911 jLL_S = S-test joint log-likelihood; N_{F/O} = forecasted/observed event ratio; IG_{CRS1} = information
 912 gain on CRS1-*basic*.

913

914

915

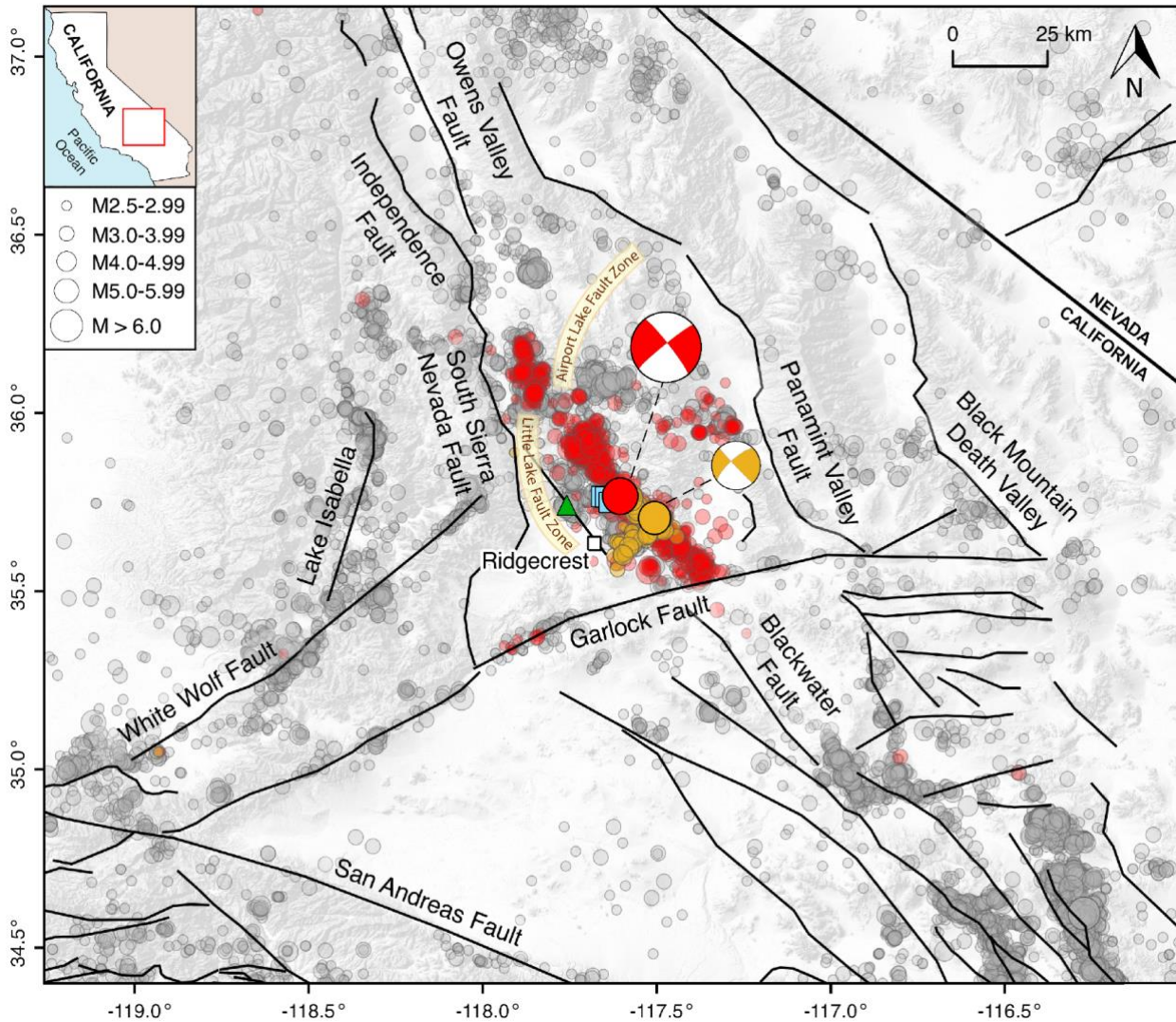
916

917

918

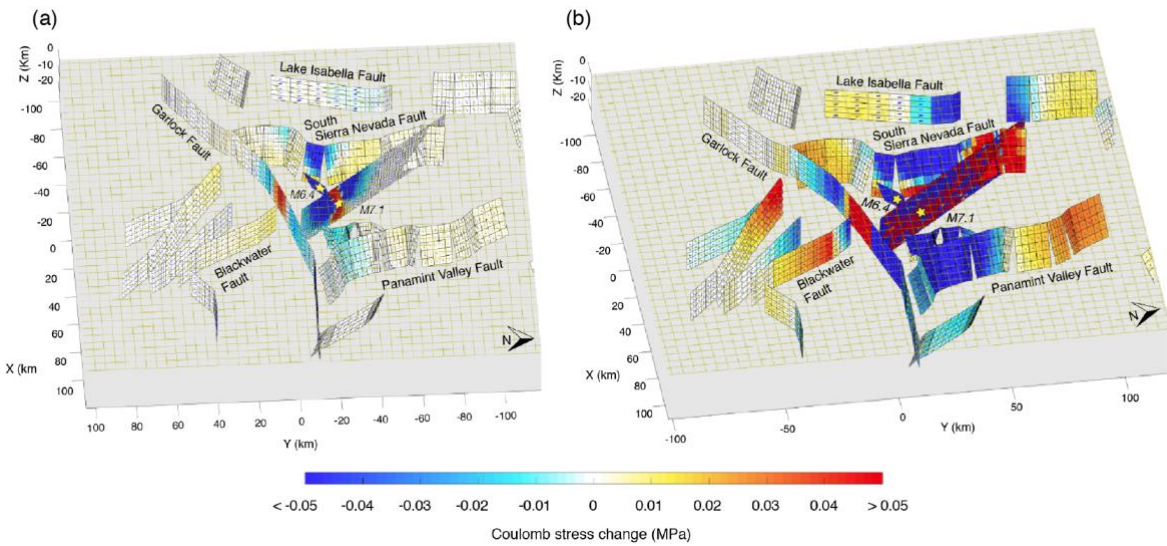
919

920 **Figures with captions**



921
 922 **Figure 1.** Testing region map. Earthquakes with M2.5+ are shown: pre-Ridgecrest (1981-2019,
 923 grey circles), post Mw 6.4 Searles Valley event (orange), post Mw 7.1 Ridgecrest mainshock (red).
 924 We report the focal mechanisms of the two mainshocks. The 1 October 1982 Indian Wells event
 925 (M=5.2) is indicated as a green triangle. Light blue squares represent the epicenters of the 1995-
 926 1996 Ridgecrest sequence mainshocks (M=5.4, 17 August 1995; M=5.8, 20 September 1995;
 927 M=5.2, 7 January 1996). The 1995 Ridgecrest sequence activated a number of normal, left and
 928 right-lateral faults. Black solid lines indicate the UCERF3 (*Dawson, 2013*) fault traces.

929
 930
 931
 932
 933



934
 935 **Figure 2.** Example of calculated combined coseismic stress changes on mapped UCERF3 faults
 936 following (a) the 4 July 2019 Mw 6.4 event and (b) both the Mw 6.4 and 6 July Mw 7.1 earthquakes
 937 near Ridgecrest, CA. Hypocenters of the Mw 6.4 and Mw 7.1 earthquakes are shown by yellow
 938 stars. Displayed stress changes were calculated using a friction coefficient of 0.4. Stress increases
 939 ($\Delta\text{CFF} \geq 0.01$ MPa) are calculated on the Central Garlock, South Sierra Nevada, Owens Valley,
 940 Tank Canyon, and Panamint Valley faults (Table S2).

941

942

943

944

945

946

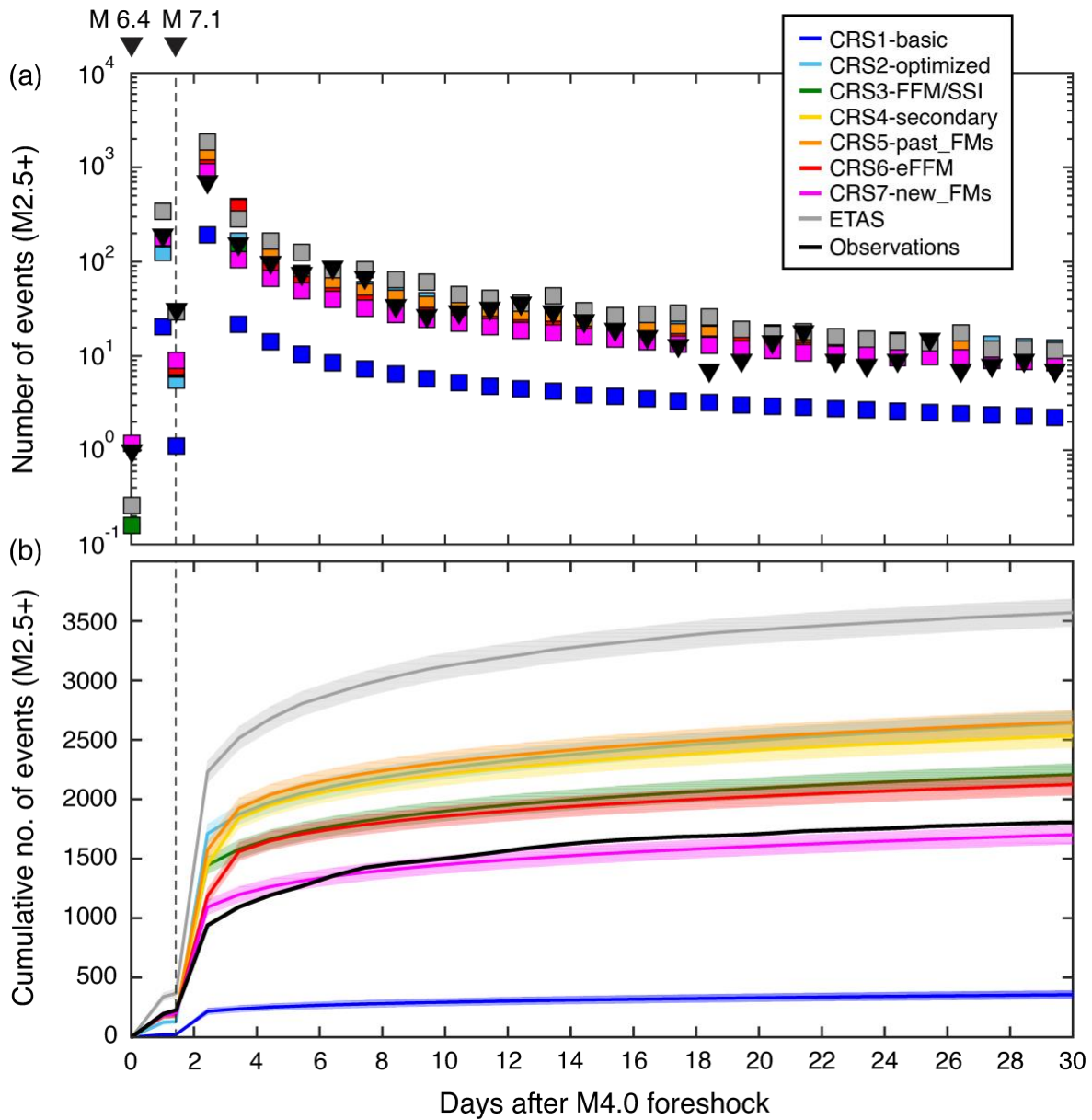
947

948

949

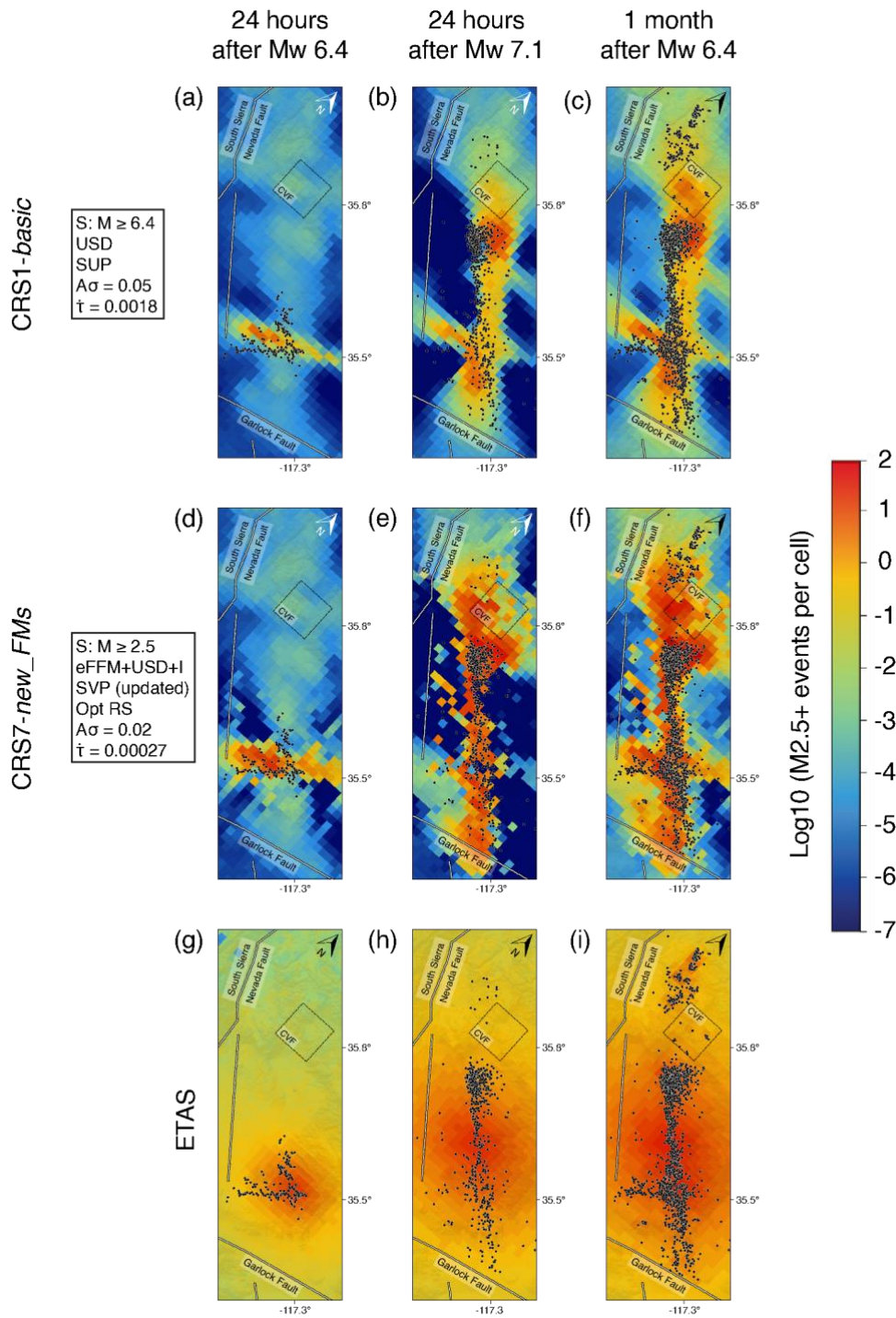
950

951



952

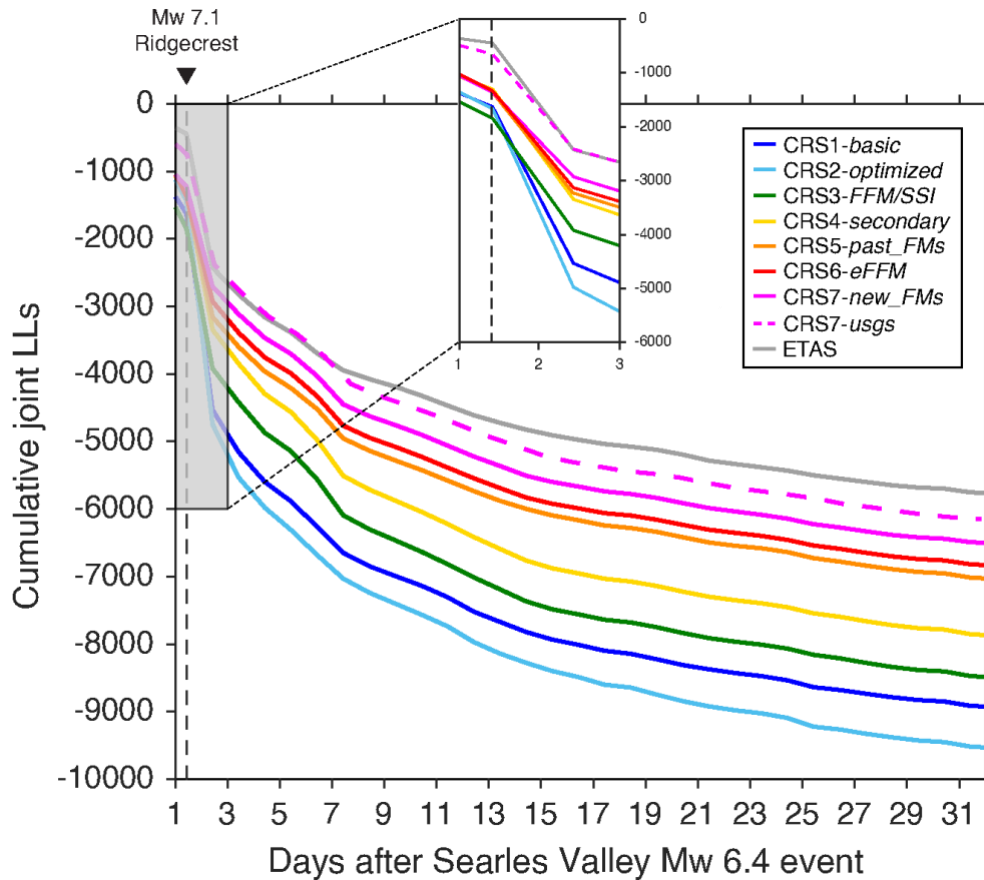
953 **Figure 3.** Forecast time series for physics-based and statistical models for the first month of the
 954 Ridgecrest sequence. (a) Incremental time series: black triangles indicate the observed number of
 955 M2.5+ events, while squares represent the expected numbers. (b) Comparison between the
 956 cumulative expected vs. observed (black line) rates. The shaded areas indicate Poissonian
 957 uncertainties.



958

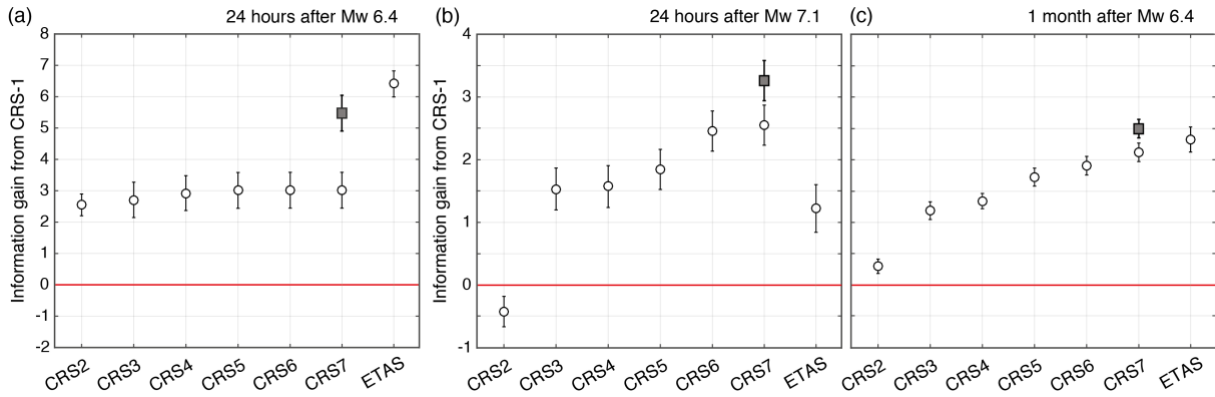
959 **Figure 4.** Maps of expected seismicity rates for CRS1/7 and ETAS in the area of main aftershock
 960 productivity for the first 24 hours following the two mainshocks and for the first month of the
 961 Ridgecrest sequence. Observed events (M2.5+) in each time window are represented as circles.

962 The dashed-line square indicates the area of the Coso volcanic field (CVF). S = sources (minimum
 963 magnitude); Opt RS = optimized rate-and-state parameters, USD = uniform slip distribution; SUP
 964 = spatially uniform receiver planes; SVP = spatially variable planes; eFFM = edited finite-fault
 965 slip model; I = isotropic stress field. $A\sigma$ values are in MPa, $\dot{\tau}$ values are in MPa/year.
 966
 967
 968



969 **Figure 5.** Cumulative S-test joint log-likelihood (jLL_S) timeseries. The scores are obtained by
 970 summing the S-test log-likelihoods (LL_S) of each spatial cell and 1-day time step. The vertical
 971 dashed line marks the occurrence of the Ridgecrest mainshock.
 972

973



974

975

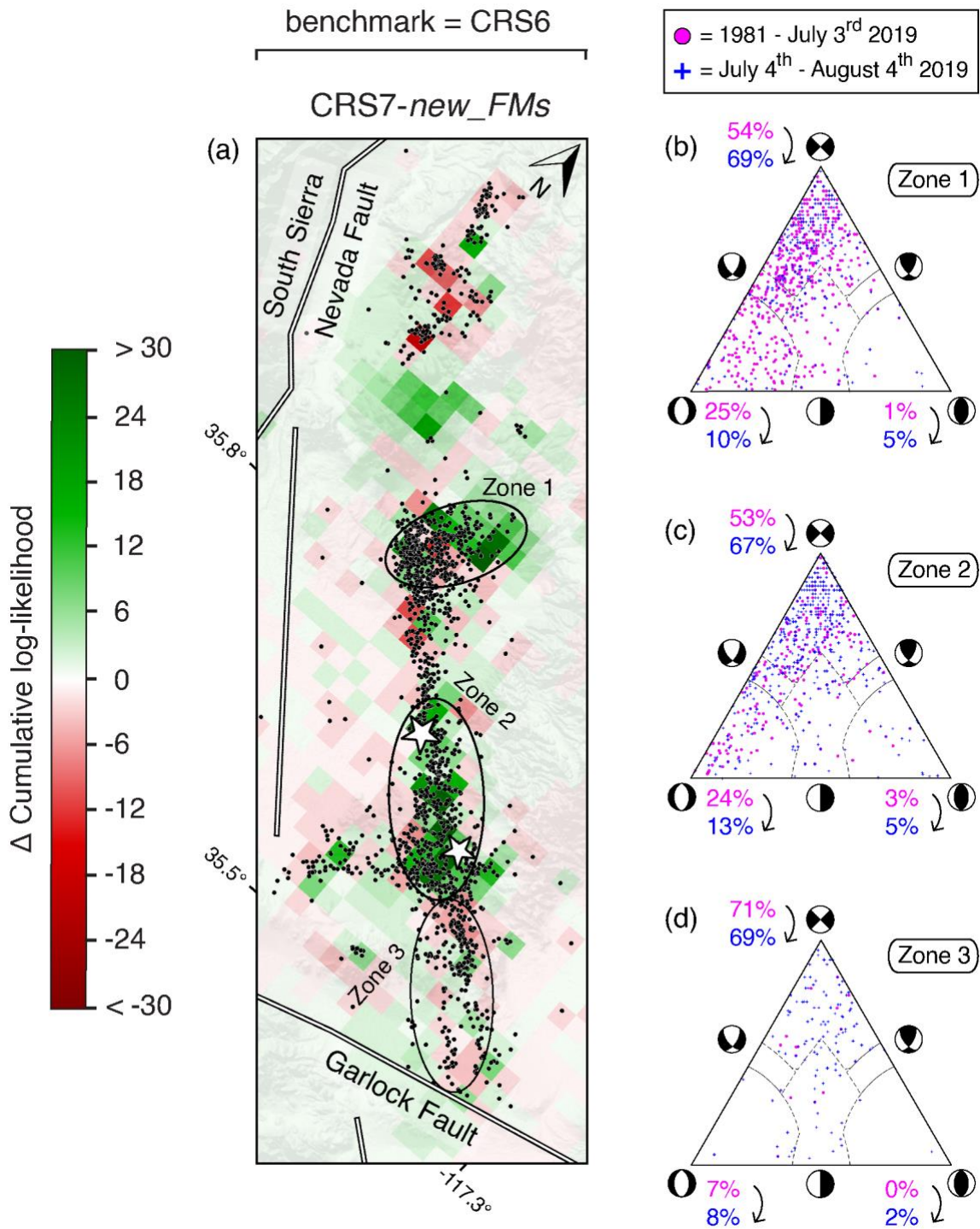
976

977

978

979

Figure 6. Average daily information gain per earthquake from the preliminary CRS1-*basic* model for: (a) 24 hour after the Mw 6.4 Searles Valley event, (b) 24 hour after the Mw 7.1 Ridgecrest mainshock and (c) for a cumulative 1-month forecast horizon. The filled grey squares indicate the information gain score of the alternative CRS7-*usgs* model. The horizontal lines mark the no-gain level.



980

981 **Figure 7.** Influence of pre-existing and evolving rupture populations in stress-based forecasts. (a)
 982 Map of cumulative Δ LL for the 1-month forecast horizon between CRS6-eFFM and CRS7-
 983 new_FMs. Positive (green) values indicate a better performance of CRS7-new_FMs. Black points
 984 indicate the locations of M2.5+ aftershocks between 4 July 2019 and 4 August 2019, while white

985 stars represent the two mainshocks. Values are saturated at ± 30 to facilitate visualization. (b-d)
986 Ternary diagrams showing the distribution of focal mechanisms during the pre-sequence (1981-
987 2019, magenta circles) and post-Ridgecrest (blue crosses) time windows.